Above-threshold ionization in a strong dc electric field

Y. Ni,[1] S. Zamith,[1,2] F. Lépine,[1] T. Martchenko,[1] M. Kling,[1] O. Ghafur,[1] H. G. Muller,[1] G. Berden,[3] F. Robicheaux,[4] and M. J. J. Vrakking[1]

[1]*FOM Institute for Atomic and Molecular Physics, Kruislaan 407, 1098 SJ Amsterdam, The Netherlands*

[2]*Laboratoire Collisions, Agrégats, Réactivité (UMR 5589, CNRS-Université de Toulouse, UPS), IRSAMC, Toulouse, France*

[3]*FOM Institute for Plasma Physics, Rijnhuizen Edisonbaan 14, 3439 MN Nieuwegein, The Netherlands*

[4]*Department of Physics, Auburn University, Auburn, Alabama 36849, USA*

(Received 17 October 2006; revised manuscript received 3 November 2007; published 18 July 2008)

High-lying Rydberg states of Xe have been ionized using intense 108 μm radiation from a free-electron laser. Measured two-dimensional photoelectron images reveal significant above-threshold ionization and contain an indirect contribution resulting from the combined action of the atomic Coulomb field, laser field, and dc electric field of the spectrometer on the electron. The observation of indirect ionization contains information about the electron localization directly after the laser excitation and indicates that the experiments are performed in the multiphoton regime of strong-field ionization. The experiments are compared to and interpreted by means of both classical and quantum-mechanical simulations.

DOI: 10.1103/PhysRevA.78.013413 PACS number(s): 32.80.Rm, 07.81.+a, 32.80.Fb, 41.60.Cr

I. INTRODUCTION

Strong-field laser ionization plays a crucial role in a number of experiments that have recently attracted considerable attention. Recollisions of electrons produced by strong-field ionization are at the basis of the process of high-harmonic generation where extreme ultraviolet (XUV) radiation is produced with a time structure in the attosecond domain [1], can probe structure and dynamics in molecular clock experiments [2], and allows the reconstruction of ground-state electronic wave functions, which leave their signature on the high-harmonic spectrum [3]. Furthermore, strong-field laser ionization can be used to monitor the dynamics of bound electrons on attosecond time scales [4]. The interpretation and further development of experiments such as these relies on a thorough understanding of strong field laser ionization and an assessment of the validity of different ionization mechanisms that are invoked.

Ionization of atoms and molecules in an intense laser field is commonly described in terms of one of two physical mechanisms: namely, multiphoton ionization or field ionization. In the multiphoton ionization regime, the ionization yield scales as $S \sim I_{\mathrm{laser}}^{N}$, where I_{laser} is the intensity of the laser and N represents the minimum number of photons needed to cross the ionization threshold. In the field-ionization regime, ionization occurs by passing over or tunneling through the barrier that results from combining the atomic Coulomb potential and the laser electric field. The transition from the multiphoton to the field-ionization regime is commonly related to the value of the Keldysh parameter $\gamma=(V_{\mathrm{ion}}/2U_p)^{1/2}$, where V_{ion} is the ionization potential of the atom and where the ponderomotive energy U_p corresponds to the kinetic energy of a free electron in the laser field. Throughout this paper we will use atomic units unless specified otherwise. In terms of the laser electric field strength F_{laser} and frequency ω, the ponderomotive energy is then expressed as $U_p=F_{\mathrm{laser}}^2/4\omega^2$. In the ionization of ground-state atoms or molecules using visible or near-infrared radiation, $\gamma \gg 1$ implies multiphoton ionization, while for $\gamma \ll 1$ ionization proceeds by tunneling or over-the-barrier ionization. Around $\gamma=1$, nonadiabatic tunneling processes are important, where the electron spends a significant amount of time (several half-cycles of the exciting laser field) in the classically forbidden region [5]. The development of new light sources allows high-intensity laser experiments in hitherto inaccessible wavelength domains. At newly developed XUV and x-ray free-electron lasers (FELs) intensities up to 10^{16} W/cm^2 have been realized at photon frequencies comparable to or larger than the atomic ionization potential, leading to dramatically different and as-yet not fully explained behavior [6]. In this paper we report photoelectron imaging experiments at far-infrared wavelengths ($\lambda=108$ μm, $\omega=4.2\times10^{-4}$ a.u.), where resolved above-threshold ionization (ATI) peaks are observed and where our experiment contains a unique observable indicating the contribution arising from ionization near the nucleus.

Experimental observables that can distinguish multiphoton or field ionization are scarce. Freeman resonances are commonly viewed as indicators of multiphoton ionization. They occur in photoelectron spectra when multiphoton excitation leads to a population of Rydberg states which are subsequently ionized. However, in focal volume-averaged experiments Freeman resonances continue to dominate the photoelectron spectra when one moves into the tunneling and over-the-barrier regime [7]. Conversely, cutoffs in the photoelectron spectrum at characteristic kinetic energies of $2U_p$ or $10U_p$ can be understood in terms of laser acceleration of electrons following field ionization [8,9], but are often not very clearly observed.

A few years ago, we reported experiments where Xe atoms were ionized in the presence of a dc electric field. A tunable, narrow-bandwidth laser was tuned between the saddle point in the Coulomb+dc field potential and the field-free ionization limit of the atom (see Fig. 1). The dc field was used to project ionized electrons onto a two-dimensional imaging detector [10,11]. Both "direct" and "indirect" electron trajectories were observed that could be distinguished by the maximum radius on the detector up to which they were detected. Direct trajectories correspond to electrons reaching the detector without further interaction with the ionic core (formally, without recrossing the electric field axis [12]),

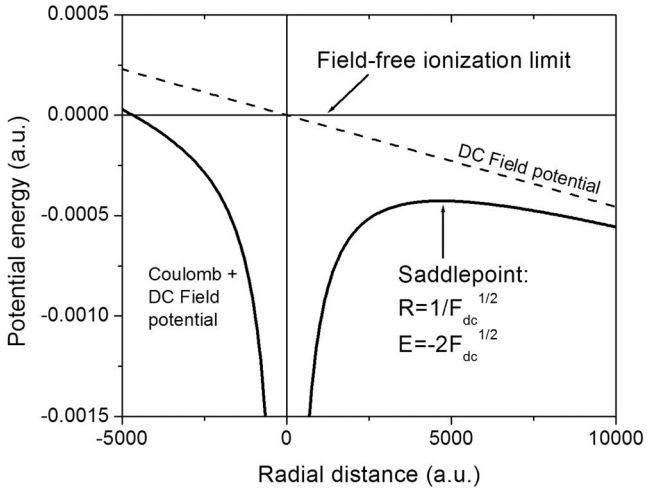

FIG. 1. Ionization in the presence of an attractive Coulomb potential and a dc electric field F_{dc} (solid line). The dc electric field (dashed line) lowers the ionization potential from its field-free value to an energy $E=-2\sqrt{F_{dc}}$. The figure is drawn for the experimental field strength $F_{dc}=4.57\times10^{-8}$ a.u. For this field strength the location of the saddle point in the Coulomb+dc field potential occurs at $R=1\sqrt{F_{dc}}=4.7\times10^{3}$ a.u. Importantly, this distance is significantly larger than the radius that the electron can reach under the influence of the 108-μm ionizing laser field, ruling out that tunneling and over-the-barrier ionization plays a role in the experiment (see text for details).

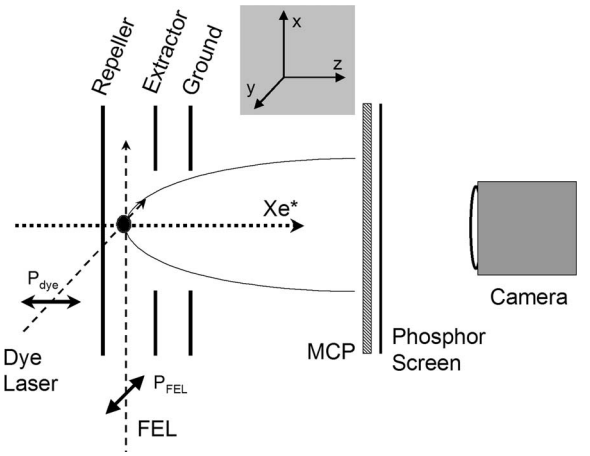

FIG. 2. Experimental arrangement: The dye laser and the FEL move at right angles with respect to each other and with respect to a Xe^* beam that moves along the detector axis of a velocity map imaging spectrometer. The polarization of the dye laser, P_{dye}, is perpendicular to the plane of the imaging detector, while the polarization of the free-electron laser, P_{FEL}, is in the plane of the imaging detector. This allows recovery of the 3D velocity distribution of the detected electrons by means of an Abel inversion as long as the electron angular distribution does not depend on the dc electric field (see text for details).

while indirect trajectories correspond to ionization events where the electron is strongly influenced by post-collision interactions with the parent ion [12]. Importantly, the experiments could be modeled (semi)classically in terms of electron trajectories that have their origin at the nucleus. It follows that the observation of these indirect trajectories in a strong-field laser ionization experiment can be viewed as evidence for the importance of ionization near the nucleus and hence the importance of the multiphoton ionization mechanism.

In the present paper experimental results on strong-field ionization of high Rydberg states using a 108-μm (i.e., far-infrared) free-electron laser will be presented. Measured photoelectron images contain evidence of indirect trajectories, signifying the importance of the interaction of the ionizing electron with the core in the course of the ionization event. Our interpretation of the experiment is supported by classical and quantum-mechanical calculations.

II. EXPERIMENT

Our experiments were performed at the FELIX (Free Electron Laser for Infrared eXperiments) facility in Nieuwegein (The Netherlands). A beam of metastable $Xe^*(6s[3/2]_{J=2})$ atoms was created using electron-impact excitation and propagated along the symmetry axis (see Fig. 2) of a velocity map imaging spectrometer. The Xe^* beam was crossed at right angles by the moderately focused output from a Lambda Physik Scanmate dye laser. A small fraction of the Xe^* atoms was excited to high-lying Rydberg states ($n\geq20$) by two-photon excitation, without leading to significant ionization. After a short delay ($\sim$10 ns), the Xe Rydberg states were ionized using an isolated 108-μm ($\Delta\lambda=2$ μm) FELIX pulse that was sliced out of the 4-μs-long FELIX macropulse using an optical switch consisting of a Si slab illuminated by a synchronized frequency-doubled Nd:YAG laser. The FELIX pulse propagated at right angles with respect to both the Xe^* beam and the dye laser beam was polarized in the plane of the two-dimensional (2D) imaging detector and was focused using an $f/10$ off-axis parabolic mirror. Assuming a transform-limited pulse duration ($\sim$5 ps) and diffraction-limited focusing of the beam, the peak intensity in the experiment was estimated to be as high as 10^7 W/cm^2. The photoelectrons were accelerated in a $F_{dc}=235$ V/cm (4.57×10^{-8} a.u.) extraction field and projected onto a dual microchannel-plate assembly followed by a phosphor screen and a camera system. The field geometry of the extraction optics allowed operation of the electron optics in velocity-map imaging (VMI) mode [13], where the (x,y) position of electrons on the detector is determined by the velocity components (v_x,v_y) of the ejected photoelectron independent of the position in the laser focus where the photoelectron is created.

III. EXPERIMENTAL RESULTS

Images were recorded while varying the wavelength of the tunable dye laser and thereby the energy of the Rydberg state that was subsequently ionized by the FEL. Selected images are shown in Fig. 3. In all the images a series of concentric rings can be observed, which correspond to different ATI orders. The photoelectron emission is preferentially along the far-infrared laser polarization axis, which is the vertical axis in the images. Since the images represent a

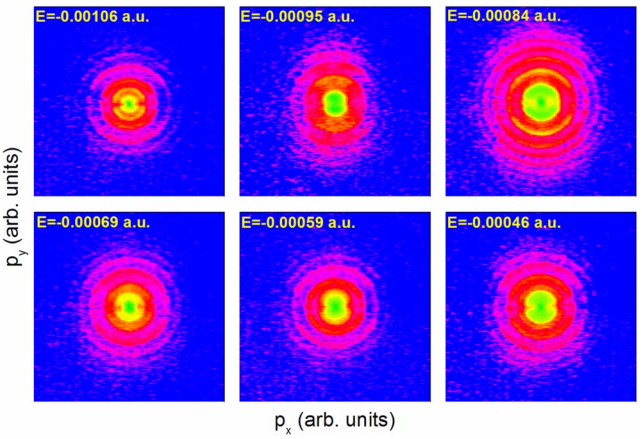

FIG. 3. (Color online) Experimental 2D images measured for ionization by the 108-μm FEL of Xe atoms that have first been prepared at a range of initial energies (given with respect to the field-free ionization limit) by tuning the wavelength of a dye laser that excited $Xe^*(6s[3/2]_{J=2})$ atoms produced by electron-impact excitation. The polarization of the FEL is along the vertical axis. The experiment was performed in a dc electric field of 235 V/cm (4.57×10^{-8} a.u.), leading to a saddle point in the Coulomb+dc field potential (see Fig. 1) at an energy of −0.000 42 a.u.

measurement of the velocity of the electron in the plane of the detector, the radial distributions are plotted in Fig. 4 as a function of the "in-plane" kinetic energy $E=\frac{1}{2}m(v_x^2+v_y^2)$. In traditional velocity-map-imaging experiments the projection of monoenergetic and isotropically emitted photoelectrons leads to the formation of a sharp ring at a velocity in the plane of the detector that corresponds to the total energy.[1] Likewise, in Fig. 4 regularly spaced peaks separated by the FELIX photon energy ($\omega=4.2\times10^{-4}$ a.u.) are observed and identified as ATI peaks. Remarkably, in several of the images an additional peak (indicated by a star) is observed between the lowest-order photoelectron peak and the first ATI peak.

To determine the possible origins of this peak, we should note that at the dc field strength used, the location of the saddle-point in the Coulomb+dc field potential lies at a distance of $1/\sqrt{F_{dc}}=4.7\times10^3$ a.u. from the nucleus. This number is to be compared to the radius of the Rydberg state from which the ionization starts, as well as the quiver amplitude of the Rydberg electron in the laser field. At the highest energy shown in Figs. 3 and 4 ($E=-0.000\,46$ a.u., where the effective principal quantum number $n^*=33.0$), the radius of the Rydberg orbital is $n^{*2}\approx1090$ a.u. For this value of the principal quantum number the radial period $2\pi n^{*3}=5.4$ ps, whereas the angular precession period in the dc electric field is $2\pi/(3Fn^*)=33.6$ ps. It follows that the experiment is performed in the high-frequency limit, where the electron cannot adiabatically respond to the driving laser field ($T_{laser}=2\pi/\omega\approx360$ fs), but performs a quiver motion in the field with amplitude $\alpha_0=F_{laser}/\omega^2$. At an intensity of 10^7 W/cm^2 ($F_{laser}=1.69\times10^{-5}$ a.u.) and $\omega=4.2\times10^{-4}$ a.u. this quiver amplitude is only equal to 96 a.u. Consequently the laser is unable to drive the electron toward the saddle-point in the Coulomb+laser field potential within the optical period of the laser. Tunneling and over-the-barrier ionization is therefore impossible, even though the strength of the laser field is sufficient to suppress the saddle point significantly below the energy of the Rydberg state. The Keldysh parameter loses its usefulness under these conditions. Even though, for the lowest energy in Figs. 3 and 4 ($E=-0.001\,06$ a.u.), γ reaches a value of 1.15 for an intensity of 10^7 W/cm^2, this does not imply that field ionization is possible.

Consequently, we argue that the newly appearing peak in Figs. 3 and 4 is the result of a post-collision interaction of the electron with its parent ion, caused by the dc electric field in the experiment. We take this peak as evidence that the ejection of the photoelectrons by the FEL includes electron trajectories that originate in a region of about 100 a.u. around the nucleus, where the gradients of the Coulomb potential are large enough to cause sufficient momentum exchange with the electron. To support this conclusion both classical and quantum-mechanical simulations will be presented in the next two sections.

We note that with the exception of one measurement performed for $E=-0.001\,18$ a.u. only a single indirect branch is observed in the photoelectron spectra, whereas the number of ATI peaks is as high as 6. As confirmed in our previous experiments [10], the cone along the electric field axis that leads to indirect ionization narrows with increasing energy and eventually becomes negligible.

IV. CLASSICAL SIMULATIONS

Classical calculations can often help to understand the origin of features in quantum systems. Therefore we performed several types of classical calculations for an atom in a static electric plus strong IR field. In the conceptually simplest calculation (model A) the initial conditions of the electron were sampled randomly so that the classical distribution had the same total energy and the same spatial distribution as the initial quantum state. The classical equations of motion were then solved with the IR field first ramped on and then ramped back off. This gave results that have almost no similarity to the experiment. First, the classical calculation gives no ionization until the laser reached a threshold intensity. Second, when ionization does occur, there are *no* rings in the momentum distribution like those seen in the experiment. This is not surprising because this classical model does not incorporate the discrete final energies due to the absorption of an integer number of photons. Only at the very highest intensities, when the rings are a minor feature, would model A be expected to give results similar to experiment.

Therefore a completely different type of calculation was subsequently performed (model B). The initial conditions in

[1]In velocity map imaging it is customary to retrieve a 3D momentum distribution from the measured 2D projection, making use of the fact that the experiment contains a symmetry axis (which is usually the laser polarization axis) in the plane of the detection. In our present experiment, the dc electric field breaks the cylindrical symmetry, leading to a situation where the trajectory of an electron that departs downwards along the field direction is very different from that of an electron that departs upwards against the field direction. Hence, no attempt can be made to extract 3D momentum distributions from the 2D projections reported here.

the classical calculation were tailored to reflect the fact that photons are absorbed near the nucleus. The radial distance where the photon is absorbed can be estimated from stationary phase arguments: the photon is absorbed at the radius where the radial momentum before the photon is absorbed (when the electron has energy E and angular momentum L) matches that after the photon is absorbed (when the electron has energy $E+\omega$ and angular momentum $L+1$). This yields a radial distance of sqrt$[(L+1)/\omega]$ and, for our frequencies and using $1<L<10$, gives a radius of the order of 100 a.u. The electrons were ejected radially outward at an energy given by $E_{\text{init}}+n\omega$ at a distance of 100 a.u. from the nucleus with an equal weight for all angles. They were launched in the Coulomb plus IR field randomly in time proportional to the intensity of the IR field for one photon, intensity squared for two photons, etc. For small IR intensities, this gave rings at the correct position with no adjustable parameters. However, the rings were completely washed out even at modest intensities (for example, 10^5 W/cm^2) when the rings are strongly visible in the experiment and in the fully quantum calculations. After examining the final momentum distribution in this classical calculation, it was found that the rings are destroyed because the electron absorbs energy from the IR field.

A last calculation was performed (model C) which did give good agreement with the experiment with no adjustable parameters. In this calculation, the electron was again launched radially outward at $r\sim 100-200$ a.u. with energy $E+n\omega$. However, we now used the Kramers-Henneberger frame—i.e., the acceleration gauge. Figure 5 shows the positions of observed peaks in the radial distributions of the emitted photoelectrons as a function of the energy of the Rydberg state prepared by the dye laser, along with predictions that were calculated by means of classical trajectory calculations according to model C. The radial positions where the photoelectrons are detected can be fully understood on the basis of the model, and inspection shows that the additional peak between the lowest-order photoelectron peak and the first ATI peak is due to indirect trajectories, where the electron interacts one or more times with the nucleus before moving off toward the detector. The observation of electron trajectories that originate at the nucleus is consistent with the multiphoton picture of strong-field ionization. Only at very high fields (when the size of the quiver motion becomes comparable to the radius from which the electron is launched) is it fruitful to think of the system as a classical electron being removed from the atom by classical laser fields. At medium to low intensities, it is more fruitful to think of the electron as suddenly acquiring $n\omega$ of energy with the motion in the laser plus atomic and static fields being more accurately described in the acceleration gauge.

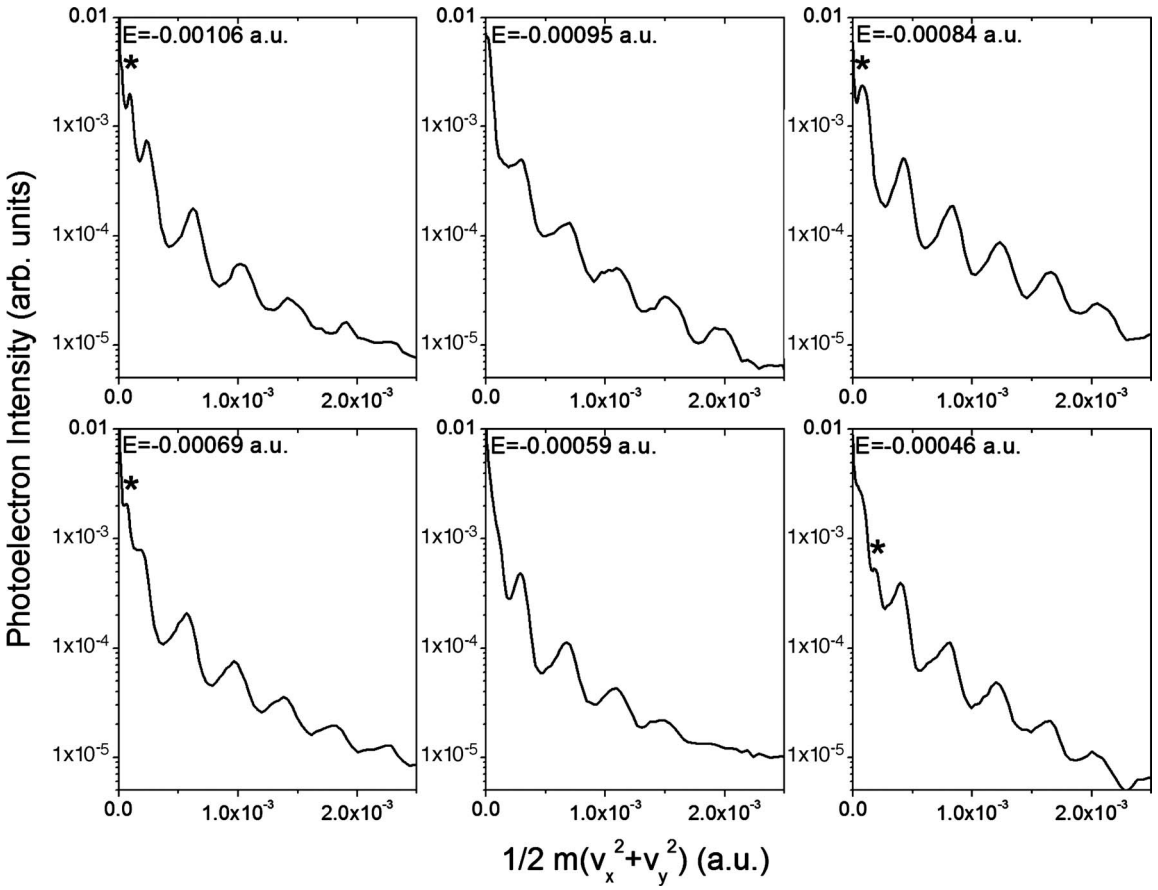

FIG. 4. Photoelectron spectra derived from the images shown in Fig. 3, showing a series of contributions corresponding to ATI, as well as indirect ionization (indicated by a star) caused by a post-collision interaction of the electron with the ion. The observation of this peak is taken as evidence that the experiment is performed in the multiphoton regime of strong-field ionization (see text for details).

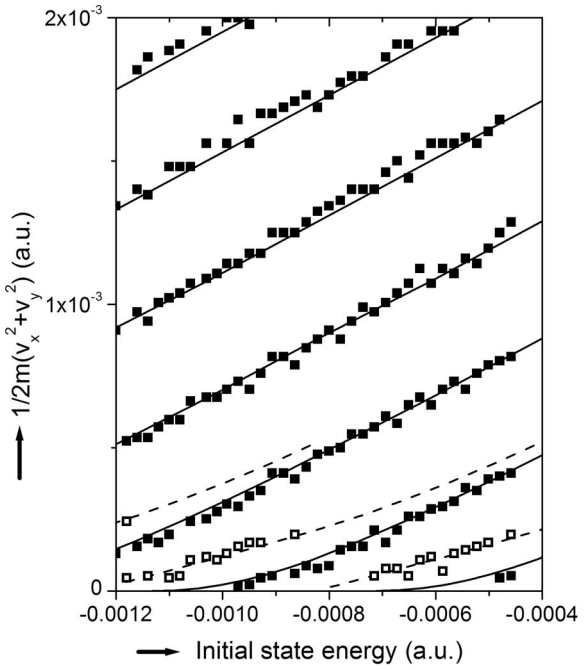

FIG. 5. Electron kinetic energies identified in the 2D photoelectron images, plotted as a function of the initial state energy used in the experiment. Branches corresponding to ATI (solid squares) and indirect ionization (open squares) are observed. The solid and dashed lines correspond to predictions from a classical theory assuming an ionization process originating at the nucleus (model C; see text for details).

V. QUANTUM-MECHANICAL SIMULATIONS

Calculations were also performed by numerically solving the time-dependent Schrödinger equation, where, to avoid a prohibitively large calculation, it was necessary to choose the laser field parallel to the dc electric field. However, since our earlier experiments indicate that dc-field-dependent post-collision interactions are similarly visible in experiments with the laser polarization parallel or perpendicular to the dc electric field axis [10], we feel justified to use this approach. The wave function of the electron was represented as a superposition of time-dependent radial functions times spherical harmonics,

$$\Psi(\vec{r},t) = \sum_l \Psi_l(\vec{r},t) Y_{l,m}(\theta,\varphi), \tag{1}$$

where the azimuthal quantum number m was held at $m=0$. The time-dependent Hamiltonian is given by $H=H_{\rm at}+[F_{\rm dc}+F_{\rm laser}(t)]z$ where $H_{\rm at}$ is the atomic Hamiltonian and $F_{\rm laser}(t)$ has the form $F_0\cos(\omega t)\exp[-(\tau/\tau_0)^4]$, where $\omega=6.0\times10^{-4}$ a.u. (corresponding to a wavelength of 76 μm) and $\tau=2$ ps were used. The initial state was formed by mimicking the experimental arrangement, with a laser pulse causing a transition to states centered at $E_{\rm init}=-8.4\times10^{-4}$ a.u. (-185 cm^{-1} with respect to the field-free ionization potential). As in the experiment, this prepares a mixture of eigenstates weighted by the two-photon matrix element with the ground state. The atomic Hamiltonian was approximated as a Numerov three-point difference on a square-root radial mesh for the kinetic energy and contained an available model potential chosen to reproduce the quantum defects of Na.[2] The atomic Hamiltonian couples adjacent radial points at fixed l, whereas the field couples l to $l\pm1$ at fixed r.

Recalling that the maximum of the Coulomb plus dc field potential is near 4.7×10^3 a.u., the calculation was performed within a sphere of radius 1.5×10^4 a.u. Calculations were performed up to a delay of 120 ps with respect to the center of the laser pulse. All of the electron flux corresponding to two or more absorbed photons and most of the flux from one absorbed photon have then left a sphere with a radius of 10^4 a.u. An absorbing mask $M(r)$ was used (after each time step) to prevent the reflection of the electron flux from the boundary of our computational region. $M(r)$ was chosen to be 1 for r less than 1.2×10^4 a.u. and goes down smoothly to 0 at the end of our radial range. In general, masks must be used with caution because there can be reflection from the mask if it turns on too abruptly or too slowly, so that flux reaches the end of the radial region. The norm of the computed wave function decreases with time due to the mask. For the situation considered in this paper, the static part of the electric field accelerates the electron, so the spread in electron velocity, which is what causes problems for masks, is manageable. The part of the wave function removed in each time step represents a small amount of outgoing probability.

The part of the wave function removed in each time step was used with a time-dependent Green's function for a linear potential to compute the asymptotic momentum distributions needed to compare with the measurements. For the case of a linear potential in the z direction, the momentum-space wave function at t_1 can be propagated to time t_2 using

$$\Phi(P_x,P_y,P_z,t_2) = \Phi(P_x,P_y,P_{1z},t_1)e^{-iS}, \tag{2}$$

where

$$P_{1z} = P_z + \int_{t_1}^{t_2} F(t)dt \tag{3}$$

and

$$S = \frac{t_2-t_1}{2}(P_x^2+P_y^2) + \frac{1}{2}\int_{t_1}^{t_2} P_z^2(t)dt, \tag{4}$$

with

$$P_z(t) = P_{1z} - \int_{t_1}^{t} F(t')dt'. \tag{5}$$

This expression was surprisingly robust and did not seem to have any instabilities. The only caution is that the integrals of $F(t)$ over t have to be done using the same order integrator

[2]Xe cannot be described by a simple model potential, since this is a multichannel problem even without external field. Calculations performed with available model potentials of K and for H atoms did not yield significant differences, though a slight dependence on the choice of the initial state was observed, and hence we judge that this calculation should be able to qualitatively reproduce the observations made in our Xe experiment.

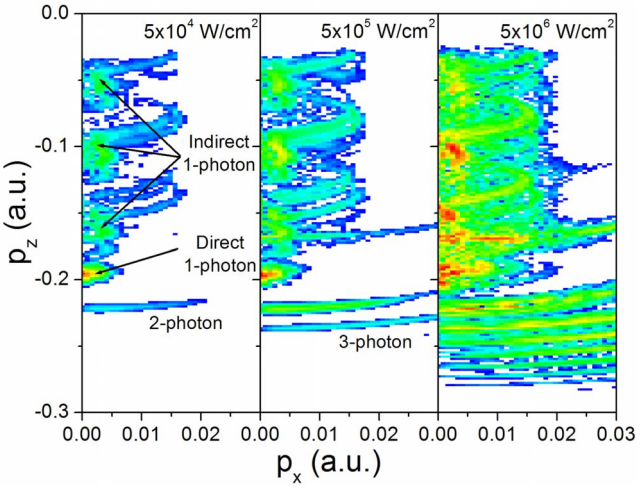

FIG. 6. (Color online) Momentum maps of the ionized electron wave packet calculated at a delay of 120 ps for ionization of Xe atoms prepared at an initial energy of −0.000 84 a.u. and ionized with a 2-ps $\omega=6\times10^{-4}$ a.u. laser pulse with a peak intensity of (a) 5×10^4 W/cm^2, (b) 5×10^5 W/cm^2, and (c) 5×10^6 W/cm^2. Contributions assigned to direct and indirect one-photon ionization and multiphoton ionization are indicated. In the momentum maps a change in the ratio of the direct-to-indirect ionization [comparing the intensity at ($p_x=0.$, $p_z=-0.19$ a.u.) to that at ($p_x=0$, $p_z=-0.10$ a.u.)] can be readily observed. Note that unlike the experiment, in the calculation both the far-infrared laser pulse and the dc electric field were polarized along the z axis.

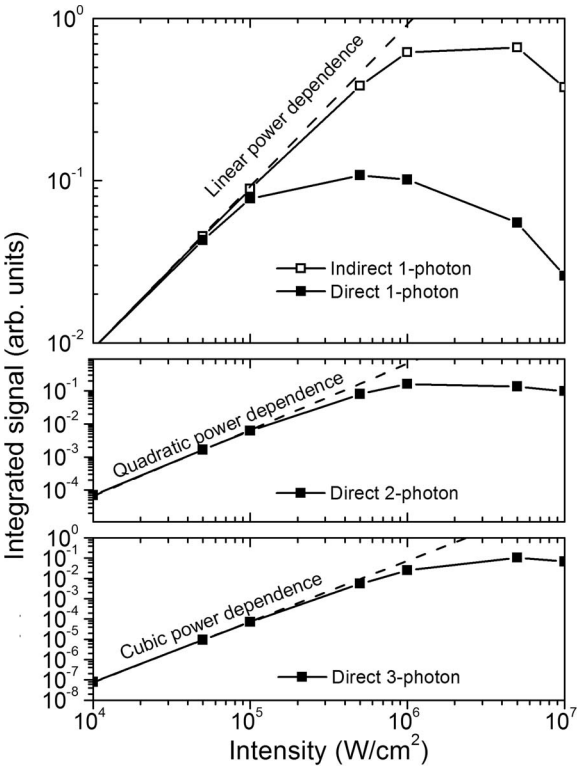

FIG. 7. Power dependence of the direct and indirect one-photon contributions to the ionization yield (scaled to a common value at low intensity), along with that of two- and three-photon contributions in the momentum maps. Importantly, the indirect one-photon contribution retains a linear power dependence well beyond the intensity ($\sim5\times10^5$ W/cm^2) where the direct contributions begins to deviate significantly

as used in the numerical propagation of the Schrödinger equation.

Hence, the sequence of operations used to obtain the momentum-space wave function was as follows. After a time step, the outgoing part of the wave function at large distance was obtained using the mask $M(r)$, according to

$$\Delta\Psi_l(\vec{r},t)=[1-M(r)]\Psi_l(\vec{r},t). \tag{6}$$

This part of the wave function goes to the detector. To use Eq. (2), we need to convert this to momentum space which is done using the radial form of the Fourier transform:

$$\Delta\Phi(P_x,P_y,P_z,t) = 2\sum_l (-i)^l Y_{lm}(\theta_p,\varphi_p)\int_0^\infty j_l(pr)\Delta\Psi_l(\vec{r},t)r^2dr. \tag{7}$$

This integration can be done very quickly because the number of nonzero points in $\Delta\Psi$ is not large. The function $\Delta\Phi(t)$ is propagated to t_{final} and the final wave function is built up by adding up all previous amplitudes. The momentum along the field is not detected, so the xy momentum distribution can be built up by taking the squared magnitude of Φ and integrating over p_z. Because of the final integration over p_z, the final time is not important as long as it is larger than or equal to the final time in the solution of the Schrödinger equation. We note that there is an approximation in this method due to our neglect of the Coulomb potential for the asymptotic approximation. This is the reason why a mask was used that only became important for distances 3 times larger than the distance to the maximum of the potential. This approximation can be controlled by having the mask start at larger r. We note that the CPU time for the calculation of the Schrödinger equation tends to increase rapidly with the size of the radial region so that in practice it would be difficult to get much larger without using parallel machines.

Figure 6 shows a series of three momentum maps for peak intensities of 5×10^4 W/cm^2, 5×10^5 W/cm^2, and 5×10^6 W/cm^2 using $\omega=6\times10^{-4}$ a.u. ($\lambda=76$ μm) and $F_{\text{dc}}=4.57\times10^{-8}$ a.u. (235 V/cm). The momentum maps show a cut (at $p_y=0$) through the 3D momentum wave function after removal of the ground state, where $p_x=0$ corresponds to the symmetry axis and where $p_z<0$ implies that the electron is moving toward the detector. Inspection of these momentum maps, aided by evaluation of the classical equations of motion, allows identification of both direct N-photon ($N=1,2,3,\ldots$) and indirect ionization processes. Specifically, the area around ($p_x=0$, $p_z=-0.19$ a.u.) is assigned to direct one-photon ionization and the area around ($p_x=0$, $p_z=-0.10$ a.u.) to indirect one-photon ionization. The calculations clearly support the coexistence of all ionization channels observed in the experimental images. In Fig. 6 the evolution of the momentum map of the ionized electrons with increasing laser intensity is shown. At higher intensity more and more ATI peaks are visible. This is further illustrated in

Fig. 7, where the relative contribution of direct and indirect one-photon, as well as two-photon and three-photon ionization is plotted as a function of the laser intensity. As expected, at low intensity ($<10^5$ W/cm^2) all contributions display a power dependence in accordance with the number of photons that are absorbed. At higher intensity, saturation sets in, since higher-order ATI processes become important, at the expense of the lower-order contributions considered here. Remarkably, the direct one-photon contribution (and, similarly, the two- and three-photon ionization channels) deviates from a linear power dependence significantly before the indirect one-photon process. This either indicates that the laser field alters the ratio of direct-to-indirect ionization trajectories (by changing the angular distribution of the emitted photoelectrons, which determines whether a trajectory will become direct or indirect [12]) or that the ionization involves a second process that reaches saturation before the ionization process near the nucleus does. However, having convinced ourselves that field ionization is not possible for our experimental parameters, there is no plausible candidate for this second process. We therefore conclude that the change in the ratio of direct-to-indirect ionization is likely caused by changes in the angular distribution of the emitted photoelectrons.

In conclusion, we have presented experiments on strong-field ionization at far-infrared wavelengths that can only be explained within the multiphoton picture of strong-field ionization. By performing the experiment in the presence of a dc electric field, contributions have been identified that are directly related to ionization near the nucleus.

ACKNOWLEDGMENTS

The skillful assistance of the FELIX staff is gratefully acknowledged. This work is part of the research program of the "Stichting voor Fundamenteel Onderzoek der Materie" (FOM), which is financially supported by the "Nederlandse organisatie voor Wetenschappelijk Onderzoek" (NWO). Financial support by the Marie Curie Research Training Networks "PICNIC" and "XTRA" is gratefully acknowledged. S.Z. and M.K. acknowledge the European Community for receiving a Marie-Curie grant. F.R. is supported by the National Science Foundation under Grant No. 0355039.

[1] P. Agostini and L. F. DiMauro, Rep. Prog. Phys. **67**, 813 (2004).
[2] H. Niikura, F. Légaré, R. Hasbani, M. Y. Ivanov, D. M. Villeneuve, and P. B. Corkum, Nature (London) **421**, 826 (2003).
[3] J. Itatani, J. Levesque, D. Zeidler, H. Niikura, H. Pepin, J. C. Kieffer, P. B. Corkum, and D. M. Villeneuve, Nature (London) **432**, 867 (2004).
[4] M. Uiberacker, Th. Uphues, M. Schultze, A. J. Verhoef, V. Yakovlev, M. F. Kling, J. Rauschenberger, N. M. Kabachnik, H. Schröder, M. Lezius, K. L. Kompa, M. J. J. Vrakking, S. Hendel, U. Kleineberg, U. Heinzmann, M. Drescher, and F. Krausz, Nature (London) **446**, 627 (2007).
[5] G. L. Yudin and M. Y. Ivanov, Phys. Rev. A **64**, 013409 (2001).
[6] A. A. Sorokin, S. V. Bobashev, T. Feigl, K. Tiedtke, H. Wabnitz, and M. Richter, Phys. Rev. Lett. **99**, 213002 (2007).
[7] T. Morishita, Z. Chen, S. Watanabe, and C. D. Lin, Phys. Rev. A **75**, 023407 (2007).
[8] P. B. Corkum, N. H. Burnett, and F. Brunel, Phys. Rev. Lett. **62**, 1259 (1989).
[9] B. Walker, B. Sheehy, K. C. Kulander, and L. F. DiMauro, Phys. Rev. Lett. **77**, 5031 (1996).
[10] C. Nicole, I. Sluimer, F. Rosca-Pruna, M. Warntjes, M. Vrakking, C. Bordas, F. Texier, and F. Robicheaux, Phys. Rev. Lett. **85**, 4024 (2000).
[11] C. Nicole, H. L. Offerhaus, M. J. J. Vrakking, F. Lépine, and C. Bordas, Phys. Rev. Lett. **88**, 133001 (2002).
[12] Ch. Bordas, Phys. Rev. A **58**, 400 (1998).
[13] A. T. J. B. Eppink and D. H. Parker, Rev. Sci. Instrum. **68**, 3477 (1997).